ARTICLE

Band-Gap Engineering *via* Tailored Line Defects in Boron-Nitride Nanoribbons, Sheets, and Nanotubes

Xiuling Li,[†] Xiaojun Wu,[†,‡,*] Xiao Cheng Zeng,[§,*] and Jinlong Yang[‡,*]

[†]CAS Key Laboratory of Materials for Energy Conversion and Department of Material Science and Engineering, University of Science and Technology of China, Hefei, Anhui 230026, People's Republic of China, [‡]Hefei National Laboratory for Physical Science at the Microscale, University of Science and Technology of China, Hefei, Anhui 230026, People's Republic of China, and [§]Department of Chemistry, University of Nebraska—Lincoln, Lincoln, Nebraska 68588, United States

ABSTRACT We perform a comprehensive study of the effects of line defects on electronic and magnetic properties of monolayer boron-nitride (BN) sheets, nanoribbons, and single-walled BN nanotubes using first-principles calculations and Born—Oppenheimer quantum molecular dynamic simulation. Although line defects divide the BN sheet (or nanotube) into domains, we show that certain line defects can lead to tailor-made edges on BN sheets (or imperfect nanotube) that can significantly reduce the band gap of the BN sheet or nanotube. In particular, we find that the line-defect-embedded zigzag BN nanoribbons (LD-zBNNRs) with chemically homogeneous edges such as B- or N-terminated edges can be realized by introducing a B_2, N_2, or C_2 pentagon—octagon—pentagon (5—8—5) line defect or through the creation of the antisite line defect. The LD-zBNNRs with only B-terminated edges are predicted to be antiferromagnetic semiconductors at the ground state, whereas the LD-zBNNRs with only N-terminated edges are metallic with degenerated antiferromagnetic and ferromagnetic states. In addition, we find that the hydrogen-passivated LD-zBNNRs as well as line-defect-embedded BN sheets (and nanotubes) are nonmagnetic semiconductors with markedly reduced band gap. The band gap reduction is attributed to the line-defect-induced impurity states. Potential applications of line-defect-embedded BN nanomaterials include nanoelectronic and spintronic devices.

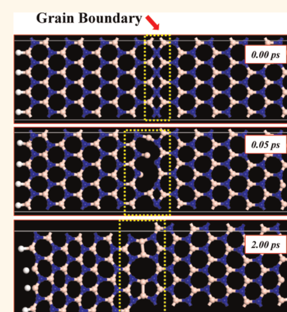

KEYWORDS: *h*-BN sheet · nanoribbon · nanotube · line defect · band gap reduction

Two-dimensional (2D) monolayer boron-nitride (BN) sheets, structural analogues of graphene, have attracted much research attention in part because 2D BN sheets are semiconductors with a wide direct band gap, while graphene is a semimetal with a zero band gap.[1−7] In particular, BN nanoribbons (BNNRs), the 1D BN nanostructures carved out of the 2D BN sheet, can present versatile electronic and magnetic properties depending on their edge structures, thereby holding great potential for nanoscale electronics and spintronics applications. BNNRs can be produced from cutting a BN sheet or by unzipping BN nanotubes in the axial direction.[8] Theoretical calculations have shown that the band gap of BNNRs with hydrogenated zigzag edges (H-zBNNRs) decreases with increasing ribbon widths, and the gap can be modulated by a transverse electric field as well.[9−11] Partial hydrogenation,[12,13] fluorination,[14−16] or oxygen functionalization [17] may convert zBNNRs into half-metals. Moreover, zBNNRs with a bare (or unpassivated) B and a bare N edge exhibit novel magnetic edge states, where the B edge is coupled antiferromagnetically whereas the N edge is coupled ferromagnetically.[18−22] Hydrogenation of the B edge of zBNNR may lead to stable half-metals and possibly half-metallic Dirac points.[18−22]

Recently, 1D extended line defects in graphene sheets have been observed experimentally, which stem from structural mismatch during the growth of graphene on a metal surface.[23−28] For example, in their experiment, Lahiri *et al*. have observed the pentagon—octagon—pentagon (5—8—5) line defect in the graphene due to the structural mismatch during growth of the graphene on the Ni(111)surface.[25] In general, the embedded line defects divide the graphene into domains with different orientations and thus can affect the electronic, thermal, and mechanical properties of graphene and graphene nanoribbons (GNRs).[26−32] A GNR containing a pentagon—heptagon (5—7) line defect may possess both armchair and zigzag edges, and various defect-dependent electron transport behaviors can be found.[26] Similarly, for the BN sheet, Auwärter *et al*. have demonstrated experimentally that the BN monolayer grown on a Ni(111) surface has two domains, which differ in the B adsorption sites (fcc or hcp for the underlying Ni substrate)

* Address correspondence to xjwu@ustc.edu.cn, xzeng1@unl.edu, jlyang@ustc.edu.cn.

Received for review February 2, 2012 and accepted April 7, 2012.

Published online April 08, 2012
10.1021/nn300495t

© 2012 American Chemical Society

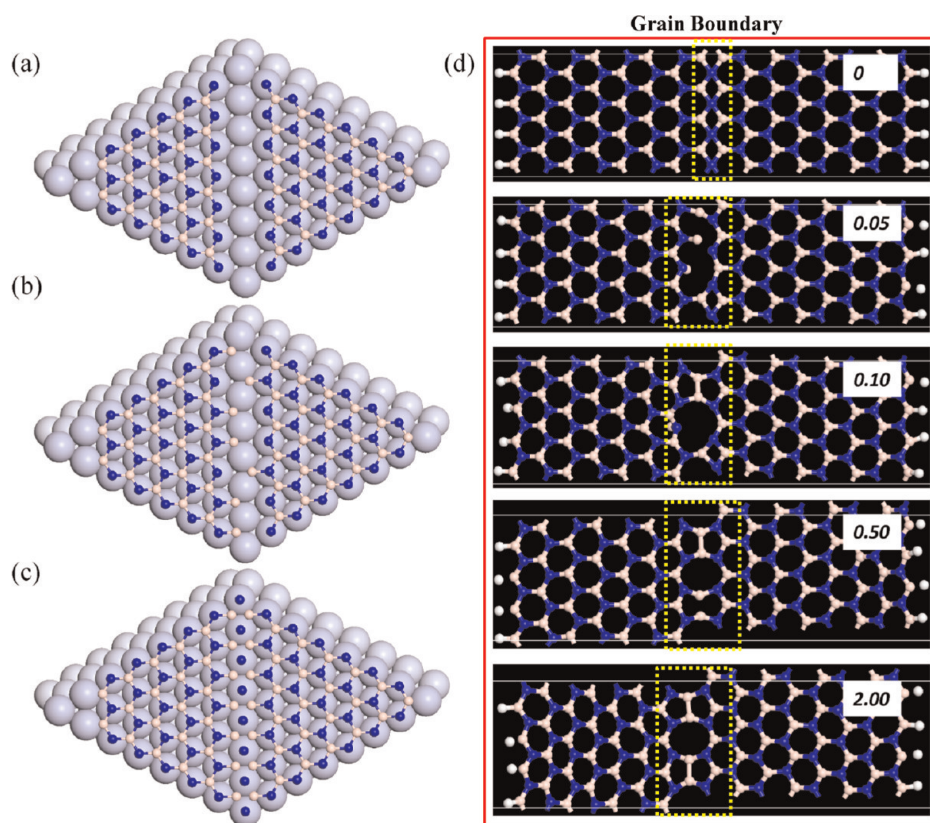

Figure 1. (a–c) Schematic structural models of a BN monolayer on the Ni(111) surface. (a) Two BN domains with different orientations (redrawn Figure 4 in ref 33). (b) Boron atoms are introduced in the gap region between two separated BN domains. (c) Boron and nitrogen atoms are introduced in the gap region following the introduction of B atoms. (d) Snapshots of zBNNRs containing a line defect in the BOMD simulation at time 0, 0.05, 0.10, 0.50, and 2.00 ps and 1000 K. The initial structure is illustrated in (c). Dark blue and light pink balls represent nitrogen and boron atoms, respectively. Big gray balls represent Ni atoms of the Ni(111) surface.

so that defect lines are present in the BN monolayer.[33] The existence of an extended line defect in a BN sheet presents a new opportunity to tune their electronic or magnetic properties in general and the band gap in particular, thus enabling the applications of BN sheet in electronics and spintronics at the nanoscale.

In this article, we report a first-principles study of the structural, electronic, and magnetic properties of line-defect-containing zBNNRs (LD-zBNNRs), BN sheets, and BN nanotubes. Born–Oppenheimer molecular dynamic (BOMD) simulation shows that a pentagon–octagon–pentagon (5–8–5) line defect can be created between two BN domains with different orientations by inserting B_2, N_2, or C_2 dimers. The antisite line defect can be also formed by connecting N or B edges between two BN domains. The LD-zBNNRs can exhibit chemically homogeneous edges, *i.e.*, having only B- or N-terminated edges. The calculations show that the band gaps of BNNRs, BN sheets, and BN nanotubes can be tuned by the line defect. The LD-zBNNRs with B-terminated edges are antiferromagnetic (AFM) semiconductors, while LD-zBNNRs with N-terminated edges are metallic with degenerated FM and AFM states. The hydrogen-passivated LD-zBNNRs as well as line-defect-embedded BN sheets (and BN nanotubes) are nonmagnetic semiconductors with markedly reduced band gaps due to the line-defect-induced impurity states. This tunability of band gaps and versatile magnetic properties extend potential applications of BN nanomaterials in nanoscale electronic and spintronic devices. In particular, the reduction of the band gap points out a possibility of making BN-monolayer-based semiconductor electronic devices in which the line defect could serve as a localized carrier-flowing channel.

RESULTS AND DISCUSSION

Previous experiments have shown that on the Ni(111) surface two types of BN domains with different orientations and B adsorption sites (either fcc or hcp for the underlying substrate) can be formed, as illustrated in Figure 1a. A very recent experiment by Kim *et al.* also demonstrates that the BN monolayer can grow into a triangular shape on a Cu surface, due possibly to the energetically favorable N-terminated edges.[34] Thus, like graphene,[25] it is possible to insert atoms, such as B, N, or C, into the grain boundary between two BN domains to create a free-standing BN sheet embedded with a line defect or line-defect-embedded BNNRs, as

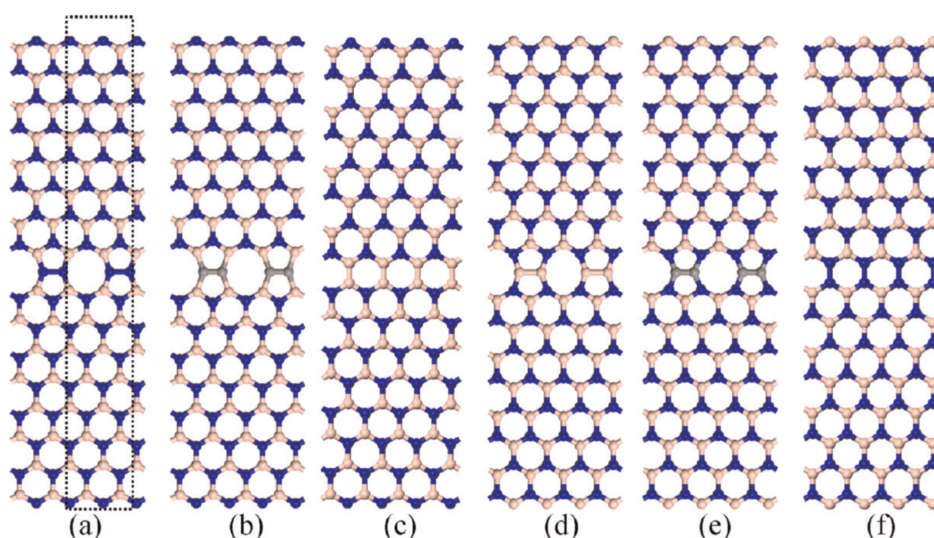

Figure 2. Optimized structures of the zBNNRs embedded with either a 5−8−5 or an antisite line defect. (a) $[NB]_8$-N_2-$[BN]_8$, (b) $[NB]_8$-C_2-$[BN]_8$, (c) $[NB]_8$-$[BN]_8$, (d) $[BN]_8$-B_2-$[NB]_8$, (e) $[BN]_8$-C_2-$[NB]_8$, and (f) $[BN]_8$-$[NB]_8$. Light pink, dark blue, and gray balls represent boron, nitrogen, and carbon atoms, respectively.

illustrated in Figure 1b and c. To verify this idea, we use the structural model shown in Figure 1c as the initial structure and perform a BOMD simulation of a free-standing zBNNR with two BN domains separated by a line defect and several B and N atoms introduced into the grain boundary (upper panels in Figure 1d). Here, the length of the supercell in the ribbon direction is four times the periodic length of the perfect zBNNR. The BOMD simulation reveals that the 5−8−5 line defect can be formed between the two BN domains with the formation of a B_2 dimer, and the nanoribbon exhibits only B-terminated edges (see Supporting Information Movie S1). Also, starting from the structural model shown in Figure 1b, geometric optimization (zero Kelvin in temperature) gives rise to a similar 5−8−5 line defect, as shown in Figure 1d. This finding suggests a way to fabricate the LD-zBNNRs with chemically homogeneous edges, *i.e.*, only B-terminated or N-terminated edges.

LD-zBNNRs with Unpassivated or Hydrogen-Passivated Edges. In Figure 2, we present a theoretical design of LD-zBNNRs with chemically homogeneous edges. We chose a perfect zBNNR with a width of 34.92 Å as the base model, which contains 16 zigzag chains along the ribbon direction. Upon cutting the ribbon into two parts, the LD-zBNNRs embedded with a 5−8−5 line defect (with mirror symmetry) can be created through connecting the two parts with B_2, N_2, or C_2 dimers, as shown in Figure 2a, b, d, and e. In the 5−8−5 line-defect-embedded LD-zBNNRs, pentagon pairs and an octagon are arranged alternatively in the ribbon axial direction. Here, we use the notation "$[BN]_8$-B_2-$[NB]_8$" to represent a LD-zBNNR with B-terminated edges and a B_2-dimer inserted into the 5−8−5 line defect (Figure 2d), where each zBNNR domain contains 8 zigzag chains in the ribbon axial direction, and the notation "$[NB]_8$-N_2-$[BN]_8$" represents a LD-zBNNR with N-terminated edges and a N_2-dimer inserted into the 5−8−5 line defect (Figure 2a). In addition to the 5−8−5 line defect, the antisite line defect can be also introduced into the zBNNRs to form the LD-zBNNRs with homogeneous edges. Such LD-zBNNRs can be constructed by connecting two zBNNRs directly in mirror symmetry, as shown in Figure 2c and f. Here, we use "$[NB]_8$-$[BN]_8$" and "$[BN]_8$-$[NB]_8$" to denote the LD-zBNNRs with B antisite and N antisite line defects, respectively.

Previous theoretical studies have predicted that the B edge is coupled antiferromagnetically and the N edge is coupled ferromagnetically for zBNNRs with

TABLE 1. Calculated Energy Band Gap (E_g), Magnetic Character of the Ground State (*G*), Total Magnetic Moment Per Unit Cell (*M*), and the Formation Energy (E_{form}) for zBNNR, H-zBNNR, LD-zBNNRs, and H-LD-zBNNRs

	E_g (eV)	*G*	*M* (μ_B)	E_{form} (eV)
zBNNR	0	$(+ + + -)^a$	1.86	
$[BN]_8$-$[NB]_8$	2.62	$(+ - + -)/(+ - - +)$	0	7.8
$[BN]_8$-B_2-$[NB]_8$	1.54	$(+ - + -)/(+ - - +)$	0	20.2
$[BN]_8$-C_2-$[NB]_8$	2.22	$(+ - + -)/(+ - - +)$	0	16.9
$[NB]_8$-$[BN]_8$	0	$(+ + + +)/(+ + - -)$	4/0	8.9
$[NB]_8$-C_2-$[BN]_8$	0	$(+ + + +)/(+ + - -)$	4/0	16.9
$[NB]_8$-N_2-$[BN]_8$	0	$(+ + + +)/(+ + - -)$	4/0	11.5
H-zBNNR	3.99	NM	0	
H$[BN]_8$-$[NB]_8$H	2.89	NM	0	7.9
H$[BN]_8$-B_2-$[NB]_8$H	2.81	NM	0	20.3
H$[BN]_8$-C_2-$[NB]_8$H	2.23	NM	0	17.1
H$[NB]_8$-$[BN]_8$H	3.02	NM	0	10.4
H$[NB]_8$-C_2-$[BN]_8$H	2.00	NM	0	18.7
H$[NB]_8$-N_2-$[BN]_8$H	3.53	NM	0	13.2

[a] The $(+ + + -)$ means the FM order $(+ +)$ at the N edge and AFM order $(+ -)$ at the B edge.

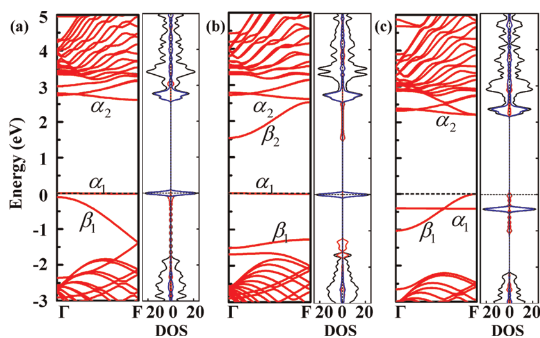

Figure 3. Computed band structures, total DOS, and PDOS of (a) $[BN]_8$-$[NB]_8$, (b) $[BN]_8$-B_2-$[NB]_8$, and (c) $[BN]_8$-C_2-$[NB]_8$. The Fermi level is set as zero. Black, blue, and red lines in the DOS represent the total DOS, PDOS of edge atoms, and line-defect atoms, respectively. The α and β states are contributed by the edge atoms and line defect, respectively. Symbols Γ and F represent the (0, 0, 0) and (0, 0.5, 0) *k*-point in the first Brillouin zone.

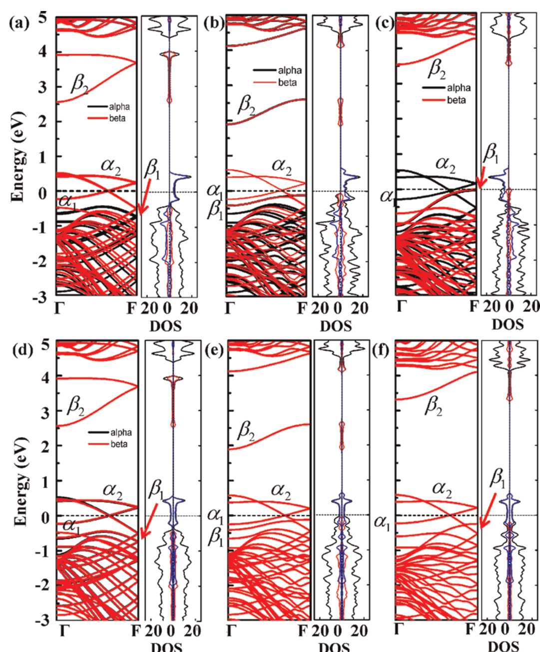

Figure 4. Computed band structures, total DOS, and PDOS of (a) $[NB]_8$-$[BN]_8$, (b) $[NB]_8$-C_2-$[BN]_8$, and (c) $[NB]_8$-N_2-$[BN]_8$ with FM (+ + + +) state and (d) $[NB]_8$-$[BN]_8$, (e) $[NB]_8$-C_2-$[BN]_8$, and (f) $[NB]_8$-N_2-$[BN]_8$ with AFM (+ + − −) state. The Fermi level is set as zero. Black, blue, and red lines in the DOS represent total DOS, PDOS of edge atoms, and line-defect atoms, respectively. The α and β states are contributed by the edge atoms and line defect, respectively. Symbols Γ and F represent the (0, 0, 0) and (0, 0.5, 0) *k*-point in the first Brillouin zone.

unpassivated edges.[18−22] The LD-zBNNRs exhibit similar magnetic order to that in perfect zBNNRs. Furthermore, the LD-zBNNRs have chemically homogeneous edge structures (either all B edge or all N edge) and thus possess richer electronic and magnetic properties. Here, we use "+ +" and "+ −" to denote the FM and AFM state of the edges. Thus, "+ + − −" represents a LD-zBNNR with two FM edges, which are coupled antiferromagnetically, and "+ + + +" represents a LD-zBNNR with two FM edges, which are coupled

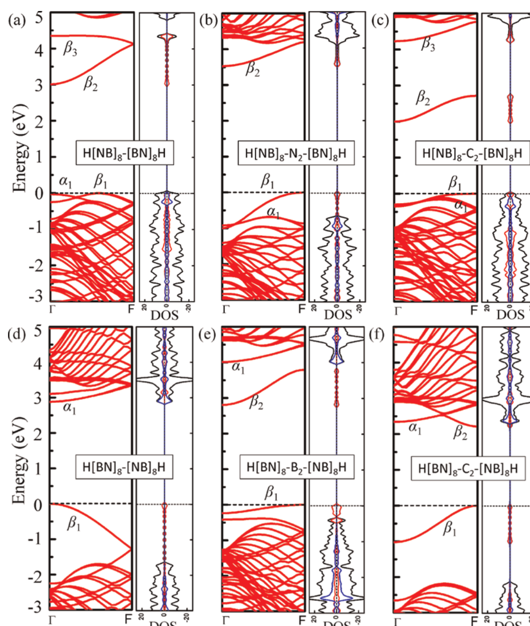

Figure 5. Calculated band structures and DOS of (a) $H[NB]_8$-$[BN]_8H$, (b) $H[NB]_8$-N_2-$[BN]_8H$, (c) $H[NB]_8$-C_2-$[BN]_8H$, (d) $H[BN]_8$-$[NB]_8H$, (e) $H[BN]_8$-B_2-$[BN]_8H$, and (f) $H[BN]_8$-C_2-$[BN]_8H$. The Fermi level is set as zero. The DOS projected on the line defect and edges are plotted in red and blue lines, respectively. Symbols Γ and F represent the (0, 0, 0) and (0, 0.5, 0) *k*-point in the first Brillouin zone.

ferromagnetically. As summarized in Table 1, for all B-edged LD-zBNNRs, including $[BN]_8$-B_2-$[NB]_8$, $[BN]_8$-C_2-$[NB]_8$, and $[BN]_8$-$[NB]_8$, the ground state is AFM with two degenerated states denoted by "+ − + −" and "+ − − +". The AFM state with the magnetic ordering denoted by "+ + − −" at B edges is less stable compared to the ground state, with the energy difference being about 0.11 to 0.12 eV per supercell. The local magnetic moment of edge B atoms is about 1.0 μ_B, and the total magnetic moment is zero based on the Mulliken population analysis.

The electronic band structures and density of states (DOS) of B-edged LD-zBNNRs are plotted in Figure 3. The B-edged LD-zBNNRs are semiconductors in their AFM ground state. The (direct) band gaps are 2.62, 1.54, and 2.22 eV for $[BN]_8$-$[NB]_8$, $[BN]_8$-B_2-$[NB]_8$, and $[BN]_8$-C_2-$[NB]_8$ LD-zBNNRs, respectively. The edged B atoms contribute a localized occupied state (α_1) without dispersion and an unoccupied state (α_2) with minor dispersion, whereas the line defect contributes either an occupied (β_1) or unoccupied (β_2) state with significant dispersion around the Fermi level, which provides a channel for the carrier transport in B-edged LD-zBNNRs. The α_1 states are σ-type degenerated states, which are distributed over the B edges, and the α_2 state is π-type orbitals (see Supporting Information Figure S1).

For the N-edged LD-zBNNRs, the ground state can be one of the two degenerate states (FM "+ + + +" and AFM "+ + − −") with the same energy.

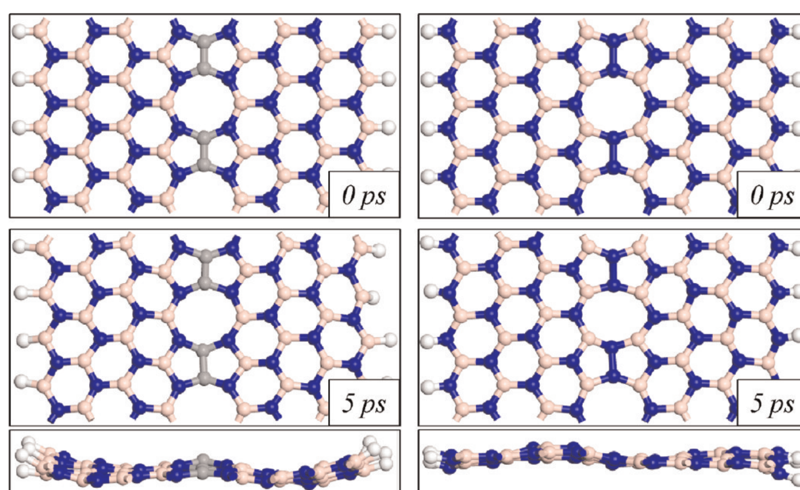

Figure 6. Snapshots of LD-zBNNRs with C_2 and N_2 5−8−5 line defects at the simulation times 0 and 5 ps with the temperature of the system being controlled at 1000 K. White, dark blue, light pink, and gray balls represent hydrogen, nitrogen, boron, and carbon atoms, respectively.

The calculated band structures indicate that the FM (+ + + +) N-edged LD-zBNNRs are half-metallic, as shown in Figure 4a−c, whereas those with the AFM (+ + − −) state are metallic, as shown in Figure 4d−f. Thus, the LD-zBNNRs with N-terminated edges exhibit paramagnetic (PM) behavior. Half-metallicity in LD-zBNNRs with N-terminated edges can be stabilized by applying an external magnetic field normal to the LD-zBNNR plane. The N atoms at all edges provide the major contribution to the DOS at the Fermi level (α_1, α_2, and α_3), while the line defect contributes the impurity states far above the Fermi level (β_1 or β_2). The versatile magnetic properties of LD-zBNNRs with bare edges may be exploited for applications in spintronic devices.

Additional calculations are performed for LD-zBNNRs whose two BN domains have different widths, *e.g.*, $[BN]_6$-$[NB]_8$ and $[BN]_6$-C_2-$[NB]_8$. The calculated band structures and DOS indicate that they possess similar electronic properties to those whose BN domains have the same width (see Supporting Information Figure S2).

Hydrogenation of all bare edges of LD-zBNNRs removes the magnetism, and the edge-hydrogenated LD-zBNNRs (denoted as H-LD-zBNNRs) become (direct or indirect) semiconductors, as summarized in Table 1. Figure 5 displays the calculated band structures and DOS of H-LD-zBNNRs. The edge states of the LD-zBNNRs move away from the Fermi level upon hydrogenation, and the H-LD-zBNNRs exhibit reduced band gaps compared with the perfect H-zBNNR (3.99 eV using the same level of theory) (see Supporting Information Figure S3). The calculated PDOS shows that the line defect yields several impurity states with large dispersion (β bands in Figure 5) within the band gap of perfect H-zBNNRs, resulting in a reduced band gap. The α and β states are contributed by the edge atoms and line defect, respectively. Furthermore, the calculated average bond energies are about 4.81 and 5.34 eV per H−N and H−B bond, respectively, which suggests that the binding of hydrogen is thermodynamically stable at the ribbons' edges.

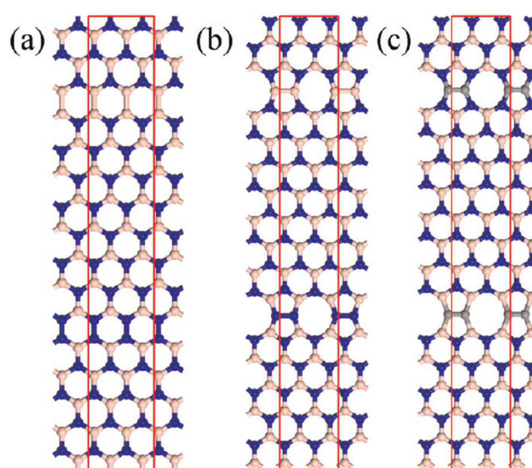

Figure 7. Optimized structures of a 2D BN sheet with (a) B and N antisite line defects, (b) B_2 and N_2 5−8−5 line defects, and (c) C_2 5−8−5 line defects.

The formation energy per supercell of LD-zBNNRs and H-LD-zBNNRs embedded with a 5−8−5 line defect is calculated based on the formula $E_{form} = 2 \times E$(zBNNR part) + E(pair) − E(LD-zBNNR), where E(LD-zBNNR), E(zBNNR part), and E(pair) are the total energies for LD-zBNNR, zBNNR part (for assembling the LD-zBNNR), and added atomic dimer, respectively. For the BN-NB LD-zBNNR, the formation energy is calculated based on $E_{form} = 2 \times E$(zBNNR part) − E(BN-NB). The calculated formation energies are summarized in Table 1. All calculated formation energies are positive, implying that the formation of LD-zBNNRs from two separated zBNNRs is exothermic and thus energetically favorable. The $[BN]_8$-B_2-$[NB]_8$ has the largest formation energy of about 20.2 eV per supercell.

To further investigate the stability of the line-defect-embedded zBNNRs, a BOMD simulation has

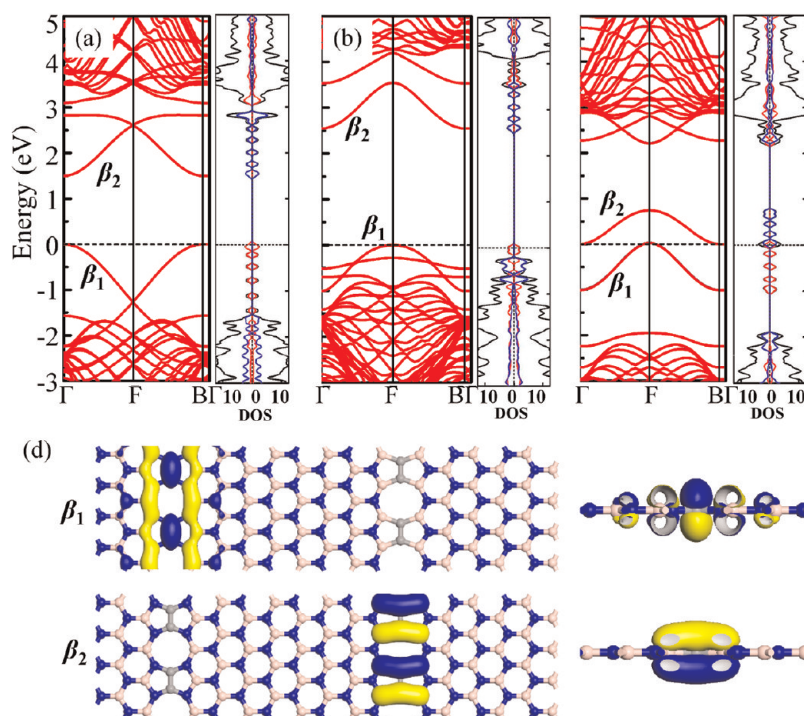

Figure 8. Computed band structures, DOS, and PDOS of a LD-BN sheet with (a) B and N antisite line defects, (b) B_2 and N_2 5−8−5 line defects, and (c) C_2 5−8−5 line defects. (d) Top and side views of the profiles of β_1 and β_2 states at the Γ point for the LD-BN sheet with a pair of C_2 5−8−5 line defects. The Fermi level is set as zero. The total DOS and PDOS on the two line defects are plotted in black, red, and blue lines, respectively. The iso-surface absolute value is 0.03 au. Symbols Γ, F, and B represent the (0, 0, 0), (0, 0.5, 0), and (0.5, 0, 0) *k*-points in the first Brillouin zone, respectively. The dark blue, light brown and gray balls represent nitrogen, boron, and carbon atoms, respectively.

been performed. The test simulations show that the embedded line defects are very stable even at a high temperature of 1000 K. In Figure 6, snapshots of the LD-zBNNRs with C_2 and N_2 5−8−5 line defects at the simulation times 0 and 5 ps are displayed. We have also performed a BOMD simulation test (total simulation time 5 ps and a time step of 1 fs) on the line-defect-embedded zBNNRs with bare edges and found the edge structures are stable at a temperature of 600 K.

Line-Defect-Embedded BN Sheet. The 2D BN monolayer-containing embedded line defects can be constructed by introducing at least two line defects in the BN sheet, such as two C_2 5−8−5 line defects or a combination of B_2 and N_2 5−8−5 line defects, as illustrated in Figure 7. The calculated band structures, total DOS, and PDOS of line defects are plotted in Figure 8. The perfect BN sheet is a semiconductor with a wide band gap of 4.77 eV (using the same level of theory). The embedded line defects introduce both occupied (β_1) and unoccupied (β_2) impurity states within the band gap of the perfect BN sheet, resulting in a remarkably reduced band gap. The LD-BN sheet with a pair of B and N antisite defects is a semiconductor with a direct band gap of about 1.50 eV. The LD-BN sheet, containing a pair of B_2 and N_2 5−8−5 line defects, is a semiconductor with an indirect band gap of about 2.52 eV. The LD-BN sheet with a pair of C_2 5−8−5 line defects is a gapless (indirect) semiconductor.[35] It is well known that the DFT-PBE method usually underestimates the band gap of the semiconductor.[36] We perform some test calculations using the HSE06 screened hybrid DFT method.[37,38] We find the LD-BN sheet with a pair of C_2 5−8−5 line defects is an indirect semiconductor with a band gap of 0.73 eV, which is significantly smaller than that of a perfect BN sheet.

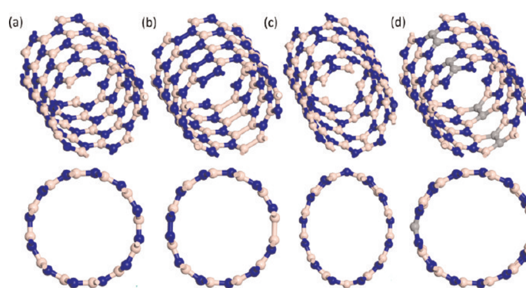

Figure 9. Optimized structures of (a) a perfect BN nanotube, (b) a BN nanotube with B and N antisite line defects, (c) a BN nanotube with B_2 and N_2 5−8−5 line defects, and (d) a BN nanotube with two C_2 5−8−5 line defects.

In Figure 8, the PDOS and profiles of states at the Γ *k*-point show that the highest occupied state (β_1) and the lowest unoccupied state (β_2) are contributed by different line defects. In the LD-BN sheet with a pair of B and N antisite line defects, the β_1 and β_2 states are contributed by N and B antisite line defects, respectively (see Supporting Information Figure S4). In a

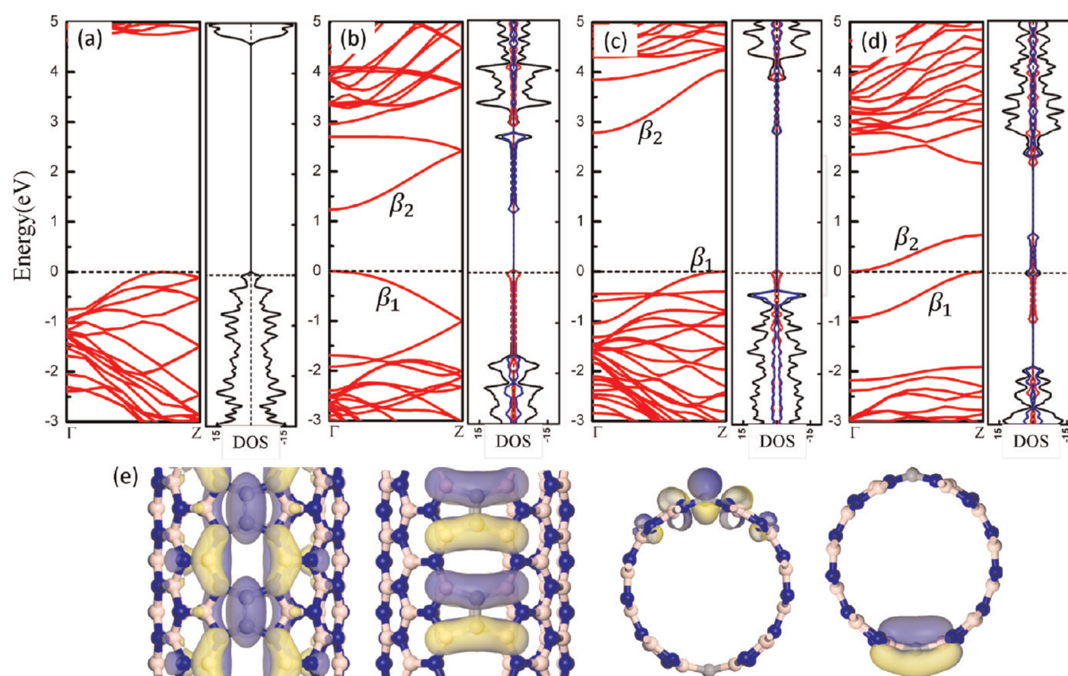

Figure 10. Calculated band structures, DOS, and PDOS of (a) a perfect BN nanotube, (b) a LD-BN nanotube with B and N antisite line defects, (c) a LD-BN nanotube with B_2 and N_2 5−8−5 line defects, and (d) a LD-BN nanotube with two C_2 5−8−5 line defects. (e) Side and top views of the profiles of β_1 and β_2 states at the Γ point for the LD-BN nanotube with a pair of C_2 5−8−5 line defects. The Fermi level is set as zero. The total DOS and PDOS on the two line defects are plotted in black, red, and blue lines, respectively. The iso-surface absolute value is 0.03 au. Symbols Γ and Z represent the (0, 0, 0) and (0, 0, 0.5) *k*-points in the first Brillouin zone, respectively.

LD-BN sheet with a pair of C_2 5−8−5 line defects, the β_1 and β_2 states are contributed by C_2 5−8−5 line defects between two N atoms and B atoms, respectively, as shown in Figure 8d. The reduction of the band gap (due to the additional line-defect-induced electronic states with strong dispersion) points out the possibility of making BN-monolayer-based semiconductor electronic devices in which the line defect could serve as a localized carrier-flowing channel.

Line-Defect-Embedded BN Nanotube. In a similar fashion, a line-defect-embedded BN nanotube (LD-BNNT) with two different domains is constructed by introducing a pair of B and N antisite defects, B_2 and N_2 5−8−5 line defects, or two C_2 5−8−5 line defects. As an example, Figure 9 displays the optimized structures of the perfect and line-defected embedded (6,6) armchair-type BN nanotubes. In contrast to the perfect BN nanotube with a circular shape (Figure 9a), the line defect induces some shape deformation on the BN nanotube. Especially, the BN nanotube with a pair of B_2 and N_2 5−8−5 line defects at opposing sites is nearly elliptical in shape (Figure 9c). Changing the location of B_2 and N_2 5−8−5 line defects within the BN nanotube will generate LD-BNNTs with various shapes (see Supporting Information Figure S5).

Calculated band structures, total DOS, and PDOS of the line defects are plotted in Figure 10. The perfect (6,6) BNNT is a semiconductor with a large band gap of ∼4.5 eV (Figure 10a). The band gaps of the LD-embedded BNNTs are significantly smaller than 4.5 eV due

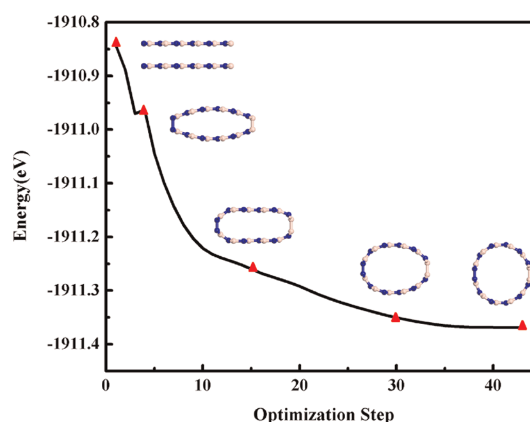

Figure 11. Energy of the LD-BN nanotube with a pair of B and N antisite defects *vs* optimization step.

to the impurity states introduced by line defects. The LD-BN nanotube with a pair of B and N antisite defects is a semiconductor with a direct band gap of ∼1.23 eV. The LD-BN nanotube containing a pair of B_2 and N_2 5−8−5 line defects is a semiconductor with an indirect band gap of ∼2.79 eV. Notably, the LD-BN tube with a pair of C_2 5−8−5 line defects is a *gapless* semiconductor (DFT-PBE calculation). The HSE06 calculation shows that the LD-BN tube with a pair of C_2 5−8−5 line defects is still a semiconductor with an indirect band gap of 0.65 eV, a value close to that for the BN sheet with C_2 5−8−5 line defects. Test calculations also show that the electronic band structures of LD-embedded BNNTs are less sensitive to the location of line defects

within the BNNT (see Supporting Information Figure S6). The PDOS and profiles of states at the Γ *k*-point indicate that the β_1 and β_2 states are mainly contributed by one of two line defects, respectively.

The formation of a LD-embedded BNNT can be realized by stacking two bare-edge BN nanoribbons in parallel. Figure 11 shows that the antisite line-defect-embedded BNNT can be formed spontaneously.

CONCLUSIONS

In conclusion, we present first-principle calculation results of a class of 1D and 2D BN nanostructures, namely, line-defect-embedded zigzag BNNRs, BN sheets, and armchair BN nanotubes. Their structural, electronic, and magnetic properties are explored for the first time. BOMD simulations suggest that a 5−8−5 line defect can be created between two BN domains with different orientations by inserting a B_2, N_2, or C_2 dimer; an antisite line defect can be created by directly connecting two zBNNRs in mirror symmetry. The LD-zBNNRs with chemically homogeneous edges possess some unique electronic and magnetic properties. The LD-zBNNRs with only B-terminated edges are predicted to be AFM semiconductors at the ground state. In contrast the LD-zBNNRs with only N-terminated edges are metallic with degenerate FM and AFM states. The FM LD-zBNNRs with N-terminated edges are half-metals. The hydrogen-passivated LD-zBNNRs as well as the line-defect-embedded BN sheets (and nanotubes) are semiconductors with notably reduced band gaps due to the impurity states induced by the line defects. The capability to significantly reduce the band gap of low-dimensional BN nanostructures through tailor-made line defects can be exploited to make BN-based nanoelectronic parts.

THEORETICAL METHODS AND MODELS

The first-principles computations are performed using the atomic orbital density-functional theory (DFT) method as implemented in the $DMol^3$ 5.5 package.[39−41] The generalized-gradient approximation in the Perdew−Burke−Ernzerhof form and the all-electron double numerical basis set augmented with polarization function are chosen for the spin-unrestricted DFT calculations.[42] The nearest distance between two neighboring nanoribbons is greater than 15 Å. The Brillouin zone is sampled by $1 \times 3 \times 1$ and $2 \times 20 \times 3$ *k*-points using the Monhkorst−Pack scheme for geometric optimization and electronic structure calculations, respectively.[43] The constant-temperature and constant-volume BOMD simulation is performed by using the Nosé−Hoover method, in which the kinetic energy fluctuation of the thermostat variable is controlled by coupling it to another thermostat variable,[44] and the temperature of the system is maintained at 1000 K.[45] The time step is 1 fs and the total simulation time is 5 ps.

Conflict of Interest: The authors declare no competing financial interest.

Acknowledgment. This work was supported by grants from NKBRPC (Grant No. 2011CB921400, 2012CB922001), NSFC (Grant No. 21121003, 11004180, 5117223), One-Hundred Talent Project of CAS, and Shanghai Supercomputer Center and Supercomputing Center of USTC. X.C.Z. is supported by grants from U.S. NSF (DMR-0820521 and EPS-1010674), ARL(W911NF1020099), and a visiting-scholar grant from USTC International Center for Quantum Design of Functional Materials.

Supporting Information Available: BOMD movie for the formation of LD-zBNNR with B_2 5−8−5 line defect, profiles of the highest occupied and lowest unoccupied states for B-terminated LD-zBNNRs, optimized structures, calculated band structures, and DOS of LD-zBNNRs with different widths for two BN domains, calculated band structures of a perfect H-zBNNR, profiles of the highest occupied state and lowest unoccupied state at the Γ *k*-point for line-defect-embedded BN sheet, and optimized structures and calculated band structures for LD-BNNT with different locations of line defects are collected. These materials are available free of charge *via* the Internet at http://pubs.acs.org.

REFERENCES AND NOTES

1. Novoselov, K. S.; Geim, A. K.; Morozov, S. V.; Jiang, D.; Zhang, Y.; Dubonos, S. V.; Grigorieva, I. V.; Firsov, A. A. Electric Field Effect in Atomically Thin Carbon Films. *Science* **2004**, *306*, 666–669.
2. Zhang, Y. B.; Tan, Y. W.; Stormer, H. L.; Kim, P. Experimental Observation of the Quantum Hall Effect and Berry's Phase in Graphene. *Nature* **2005**, *438*, 210–204.
3. Novoselov, K. S.; Jiang, D.; Schedin, F.; Booth, T. J.; Khotkevich, V. V.; Morozov, S. V.; Geim, A. K. Two-Dimensional Atomic Crystals. *Proc. Natl. Acad. Sci. U. S. A.* **2005**, *102*, 10451–10453.
4. Nag, A.; Raidongia, K.; Hembram, K. P. S. S.; Datta, R.; Waghmare, U. V.; Rao, C. N. R. Graphene Analogues of BN: Novel Synthesis and Properties. *ACS Nano* **2010**, *4*, 1539–1544.
5. Golberg, D.; Bando, Y.; Huang, Y.; Terao, T.; Mitome, M.; Tang, C.; Zhi, C. Boron Nitride Nanotubes and Nanosheets. *ACS Nano* **2010**, *4*, 2979–2993.
6. Hu, M. L.; Yu, Z. Z.; Zhang, K. W.; Sun, L. Z.; Zhong, J. X. Tunneling Magnetoresistance of Bilayer Hexagonal Boron Nitride and its Linear Response to External Uniaxial Strain. *J. Phys. Chem. C* **2011**, *115*, 8260–8264.
7. Yazyev, O. V.; Pasquarello, A. Magnetoresistive Junctions Based on Epitaxial Graphene and Hexagonal Boron Nitride. *Phys. Rev. B* **2009**, *80*, 035408.
8. Zeng, H. B.; Zhi, C. Y.; Zhang, Z. H.; Wei, X. L.; Wang, X. B.; Guo, W. L.; Bando, Y.; Golberg, D. "White Graphenes": Boron Nitride Nanoribbons *via* Boron Nitride Nanotube Unwrapping. *Nano Lett.* **2010**, *10*, 5049–5055.
9. Nakamura, J.; Nitta, T.; Natori, A. Electronic and Magnetic Properties of BNC Ribbons. *Phys. Rev. B* **2005**, *72*, 205420.
10. Zhang, Z. H.; Guo, W. L. Energy-Gap Modulation of BN Ribbons by Transverse Electric Fields: First-Principles Calculations. *Phys. Rev. B* **2008**, *77*, 075403.
11. Park, C.-H.; Louie, S. G. Energy Gaps and Stark Effect in Boron Nitride Nanoribbons. *Nano Lett.* **2008**, *8*, 2200–2203.
12. Chen, W.; Li, Y. F.; Yu, G. T.; Li, C. Z.; Zhang, S. B.; Zhou, Z.; Chen, Z. F. Hydrogenation: A Simple Approach to Realize Semiconductor−Half-Metal−Metal Transition in Boron Nitride Nanoribbons. *J. Am. Chem. Soc.* **2010**, *132*, 1699–1705.
13. Liu, Y.; Wu, X.; Zhao, Y.; Zeng, X. C.; Yang, J. L. Half-Metallicity in Hybrid Graphene/Boron Nitride Nanoribbons with Dihydrogenated Edges. *J. Phys. Chem. C* **2011**, *115*, 9442.
14. Wang, Y. L.; Ding, Y.; Ni, J. Fluorination-Induced Half-Metallicity in Zigzag Boron Nitride Nanoribbons: First-Principles Calculations. *Phys. Rev. B* **2010**, *81*, 193407.
15. Zhang, Z.; Zeng, X. C.; Guo, W. L. Fluorinating Hexagonal Boron Nitride into Diamond-Like Nanofilms with Tunable Band Gap and Ferromagnetism. *J. Am. Chem. Soc.* **2011**, *133*, 14831.

16. Zhang, Z.; Zeng, X. C.; Guo, W. L. Fluorinating Hexagonal Boron Nitride/Graphene Multilayers into Hybrid Diamond-like Nanofilms with Tunable Energy Gap. *J. Phys. Chem. C* **2011**, *115*, 21678.
17. Lopez-Bezanilla, A.; Huang, J. S.; Terrones, H.; Sumpter, B. G. Boron Nitride Nanoribbons Become Metallic. *Nano Lett.* **2011**, *11*, 3267–3273.
18. Lai, L.; Lu, J.; Wang, L.; Luo, G. F.; Zhou, J.; Qin, R.; Gao, Z. X.; Mei, W. N. Magnetic Properties of Fully Bare and Half-Bare Boron Nitride Nanoribbons. *J. Phys. Chem. C* **2009**, *113*, 2273–2276.
19. Wu, M.; Wu, X.; Pei, Y.; Zeng, X. C. Inorganic Nanoribbons with Unpassivated Zigzag Edges: Half Metallicity and Edge Reconstruction. *Nano Res.* **2011**, *4*, 233.
20. Barone, V.; Peralta, J. E. Magnetic Boron Nitride Nanoribbons with Tunable Electronic Properties. *Nano Lett.* **2008**, *8*, 2210–2214.
21. Zheng, F. W.; Zhou, G.; Liu, Z. R.; Wu, J.; Duan, W. H.; Gu, B. L.; Zhang, S. B. Half Metallicity Along the Edge of Zigzag Boron Nitride Nanoribbons. *Phys. Rev. B* **2008**, *78*, 205415.
22. Kan, E. J.; Wu, F.; Xiang, H. J.; Yang, J. L.; Whangbo, M.-H. Half-Metallic Dirac Point in B-Edge Hydrogenated BN Nanoribbons. *J. Phys. Chem. C* **2011**, *115*, 17252–17254.
23. Coraux, J.; N'Diaye, A. T.; Busse, C.; Michely, T. Structural Coherency of Graphene on Ir(111). *Nano Lett.* **2008**, *8*, 565–570.
24. Cervenka, J.; Katsnelson, M. I.; Flipse, C. F. J. Room-Temperature Ferromagnetism in Graphite Driven by Two-Dimensional Networks of Point Defects. *Nat. Phys.* **2009**, *5*, 840–844.
25. Lahiri, J.; Lin, Y.; Bozkurt, P.; Oleynik, I. I.; batzill, M. An Extended Defect in Graphene as a Metallic Wire. *Nat. Nanotechnol.* **2010**, *5*, 326–329.
26. Yazyev, O. V.; Louie, S. G. Electronic Transport in Polycrystalline Graphene. *Nat. Mater.* **2010**, *9*, 806–809.
27. Banhart, F.; Kotakoshi, J.; Krasheninnikov, A. V. Structural Defect in Graphenes. *ACS Nano* **2011**, *5*, 26–41.
28. Jeong, B. W.; Ihm, J.; Lee, G. D. Stability of Dislocation Defect with Two Pentagon-Heptagon Pairs in Graphene. *Phys. Rev. B* **2008**, *78*, 165403.
29. Yazyev, O.; Luoie, S. G. Topological Defects in Graphene: Dislocations and Grain Boundaries. *Phys. Rev. B* **2010**, *81*, 195420.
30. Malola, S.; Häkkinen, H.; Koskinen, P. Structural, Chemical, and Dynamical Trends in Graphene Grain Boundaries. *Phys. Rev. B* **2010**, *81*, 165447.
31. Kou, L. Z.; Tang, C.; Guo, W. L.; Chen, C. F. Tunable Magnetism in Strained Graphene with Topological Line Defect. *ACS Nano* **2011**, *5*, 1012–1017.
32. Okada, S.; Kawai, T.; Nakada, K. Electronic Structure of Graphene with a Topological Line Defect. *J. Phys. Soc. Jpn.* **2011**, *80*, 013709.
33. Auwärter, W.; Muntwiler, M.; Osterwalder, J.; Greber, T. Defect Lines and Two-Domain Structure of Hexagonal Boron Nitride Films on Ni(111). *Surf. Sci. Lett.* **2003**, *545*, L735–L740.
34. Kim, K.; Hsu, A.; Jia, X. T.; Kim, S. M.; Shi, Y. M.; Hofmann, M.; Nezich, D.; Rodriguez-Nieva, J. F.; Dresselhaus, M.; Palacios, T.; *et al.* Synthesis of Monolayer Hexagonal Boron Nitride on Cu Foil Using Chemical Vapor Deposition. *Nano Lett.* **2012**, *12*, 161–166.
35. Tsidil'kovskii, I. M. Gapless Semiconductors: A New Class of Substances. *Sov. Phys. Usp.* **1982**, *25*, 762–763.
36. Lany, S.; Zunger, A. Assessment of Correction Methods for the Band-Gap Problem and for Finite-Size Effects in Supercell Defect Calculations: Case Studies for ZnO and GaAs. *Phys. Rev. B* **2008**, *78*, 235104.
37. Heyd, J.; Scuseria, G. E.; Ernzerhof, M. Hybrid Functionals Based on a Screened Coulomb Potential. *J. Chem. Phys.* **2003**, *118*, 8207–8215.
38. Heyd, J.; Scuseria, G. E.; Ernzerhof, M. Erratum: "Hybrid Functionals Based on a Screened Coulomb Potential". *J. Chem. Phys.* **2006**, *124*, 219906.
39. Delley, B. An All-Electron Numerical Method for Solving the Local Density Functional for Polyatomic Molecules. *J. Chem. Phys.* **1990**, *92*, 508–517.
40. Delley, B. From Molecules to Solids with the DMol3 Approach. *J. Chem. Phys.* **2003**, *113*, 7756–7764.
41. DMol^3 5.5 is a density functional theory quantum mechanical package available from Accelrys Software Inc.
42. Perdew, J. P.; Burke, K.; Ernzerhof, M. Generalized Gradient Approximation Made Simple. *Phys. Rev. Lett.* **1996**, *77*, 3865–3868.
43. Monkhorst, H. J.; Pack, J. D. Special Points for Brillouin-Zone Integrations. *Phys. Rev. B* **1976**, *13*, 5188–5192.
44. Tuckerman, M. E.; Liu, Y.; Ciccotti, G.; Martyna, G. J. Non-Hamiltonian Molecular Dynamics: Generalizing Hamiltonian Phase Space Principles to Non-Hamiltonian Systems. *J. Chem. Phys.* **2001**, *115*, 1678–1702.
45. Nosé, S. A Molecular Dynamics Method for Simulations in the Canonical Ensemble. *Mol. Phys.* **1984**, *52*, 255–268.